ORNL/TM-2020/1658

Analysis and Design of High-Power TRISO Fuel Compact Irradiation in HFIR

R.C. Gallagher
Z. Wallen
C.M. Petrie
T. Gerczak
A. Le Coq
K. Smith
J. Harp
K. Linton

Kairos Power LLC
B. Collin
R. Latta

June 2021

OAK RIDGE National Laboratory

ORNL IS MANAGED BY UT-BATTELLE LLC FOR THE US DEPARTMENT OF ENERGY

ORNL/TM-2020/1658

Nuclear Energy and Fuel Cycle Division

ANALYSIS AND DESIGN OF HIGH-POWER TRISO FUEL COMPACT IRRADIATION IN HFIR

R.C. Gallagher
Z. Wallen
C.M. Petrie
T. Gerczak
A. LeCoq
K. Smith
J. Harp
K. Linton

Kairos Power:
B. Collin
R. Latta

June 2021

Prepared by
OAK RIDGE NATIONAL LABORATORY
Oak Ridge, TN 37831-6283
managed by
UT-BATTELLE, LLC
for the
US DEPARTMENT OF ENERGY
under contract DE-AC05-00OR22725

CONTENTS

LIST OF FIGURES

LIST OF TABLES

ABSTRACT

Tristructural isotropic (TRISO) fuel is being proposed for use in several high-temperature advanced reactor concepts because of its structural integrity under high operating temperatures and burnup. One of these advanced reactor concepts is the Kairos Power fluoride salt-cooled high-temperature reactor (KP-FHR) under development by Kairos Power, LLC. Previous TRISO irradiation experiments were focused on qualification for high-temperature gas reactors (HTGRs), which have higher operating temperatures but lower particle powers than the KP-FHR design. To study the performance of TRISO fuel designed for HTGRs under prototypical FHR conditions, a set of experiments was designed using the MiniFuel irradiation vehicle at the Oak Ridge National Laboratory's (ORNL) High Flux Isotope Reactor (HFIR). The experiments will irradiate 30 TRISO-containing carbon matrix compacts at inner small vertical experiment facilities in HFIR. Each compact will contain 20 TRISO particles (600 particles total) developed for HTGRs, consisting of either 14% enriched uranium dioxide uranium carbide, naturally enriched uranium dioxide, uranium carbide, or 9.6% enriched uranium dioxide fuel kernels with time- and volume-averaged silicon carbide layer temperatures between 500 and 900°C. This report summarizes the vehicle designs that have been developed, as well as the neutronic and thermal analyses completed for these irradiation experiments. These analyses show that MiniFuel compact irradiation is a versatile experiment that can be used to study a range of TRISO particle powers and fuel types while providing reasonable separation of burnup and temperature effects.

1. INTRODUCTION

Tristructural isotropic (TRISO) particles were primarily developed for high-temperature gas reactor (HTGR) fuel concepts owing to their structural integrity at high burnup and operating temperatures [1]. Given these performance benefits, TRISO particles and other coated particles have the potential to be adapted to a variety of advanced reactor concepts, including microreactors, nuclear thermal propulsion reactors, and molten fluoride salt-cooled reactors, as well as accident-tolerant fuel for existing light-water reactors [2, 3, 4]. High-power-density (>20 MW/m^3) TRISO particle fuels have been proposed for the Kairos Power fluoride salt-cooled high temperature reactor (KP-FHR), under development by Kairos Power, LLC [5]. The KP-FHR leverages TRISO fuel with a LiF-BeF_2 molten salt mixture (FLiBe) coolant that has improved heat transfer compared with gas coolants. This approach enables higher fuel power densities but lower operating temperatures than those in HTGRs. With power densities around five times higher than those of typical HTGR designs, which operate at around 4–6 MW/m^3, the use of high-power TRISO particles would enable a substantially reduced core size, potentially lowering the capital cost of construction [5, 6]. The irradiation performance of TRISO particles has been studied at length under the US Department of Energy's Advanced Gas Reactor (AGR) Fuel Qualification and Development Program to qualify TRISO particles for HTGRs, providing some useful data for the qualification of FHRs. However, irradiation testing of higher-power fuel particles has not been performed [1]. Therefore, an irradiation campaign was devised for accelerated testing of high-power TRISO particles developed for HTGR applications under prototypical FHR temperatures and high particle powers in the HFIR at ORNL. Those experiments will extend existing TRISO performance data, support fuel qualification for the KP-FHR, and further validate TRISO fuel performance models.

Irradiation experiments employing the miniature fuel irradiation vehicle (MiniFuel) at HFIR were designed to accommodate miniature compact specimens [7]. The MiniFuel vehicle allows for separate effects testing of fuel concepts by reducing the mass of fuel in the vehicle and, subsequently, the heat produced by fission. The temperature of the experiment is driven primarily by photon heat generated in the assembly components and therefore will be insensitive to burnup-induced changes to the fission heat generation [8]. Decoupling the temperature from the fission rate allows for key fuel performance variables like burnup, temperature, and fuel composition to be analyzed separately for their influence on

degradation phenomena. In the MiniFuel vehicle, temperature is controlled by sizing an insulating gas gap between the subcapsule containing the specimen and the target housing, which is in contact with the reactor coolant. However, testing of specimens with higher particle power densities limits the precision of temperature control that can be achieved. Thus, detailed thermal analyses were performed to predict the thermal performance of the experiments.

The TRISO particle fuel kernels to be used in the irradiation experiments described herein consist of 14% enriched uranium dioxide uranium carbide (UCO), naturally enriched uranium dioxide uranium carbide (NUCO), or 9.6% enriched uranium dioxide (UO_2), all of which were available from the existing AGR campaign lots. The AGR UCO particles have similar diameters to the fuel that will be used in the KP-FHR, and the particles are expected to reach particle powers near 1,000 mW/particle during HFIR irradiation. This peak power will be substantially higher than in previous AGR tests, which were ~100 mW/particle for AGR-1, ~150 mW/particle (UCO) and ~200 mW/particle (UO_2) for AGR-2, and ~200 mW/particle (expected) for AGR-5/6/7 [9, 10, 11]. The higher-power irradiation testing could potentially allow for higher KP-FHR powers [5]. The NUCO-containing TRISO particles are anticipated to have peak particle powers near those of previous AGR tests and will be compared with the higher-power UCO, as well as existing AGR irradiation data. Experiments at 500 and 700°C with UCO and NUCO kernels will also examine the behavior of TRISO particles at temperatures lower than those used previous AGR tests; those behaviors include the potential for buffer fracture, which appears to increase with decreasing temperature [12, 13]. Particles with UO_2 kernels and UCO kernels will also be irradiated at 900°C to verify the improved reliability of UCO kernels at higher particle powers with respect to effects like kernel migration [6]. The three design temperatures (500, 700, and 900°C), defined as the time-average and volume-average (TAVA) temperature of the TRISO silicon carbide (SiC) layers in an individual compact, were selected to provide temperature-dependent information on irradiation-induced effects; they correspond to the FHR's expected operating and off-normal temperatures.

Five MiniFuel targets—containing 30 compact specimens total—were designed and analyzed to predict their performance in HFIR for four ~24 day cycles in HFIR. With this cycle length, the fuel is expected to reach 2–12% fissions per initial metal atom (FIMA) in approximately 143 days (depending on cycle and outage length). For comparison, AGR-1 fuel reached a burnup of 11.3–19.6% FIMA in 620 effective full power days (EFPD), spanning 13 cycles and ~3 years total [10]. AGR-2 fuel reached a burnup of 9.3–12.2% FIMA in 560 EFPD, spanning 12 cycles and 3.5 years [9]. These experiments will irradiate a total of 420 UCO, 120 NUCO, and 60 UO_2 TRISO particles. The work described herein presents the mechanical design, neutronic analyses, and thermal analysis completed for this set of miniature fuel irradiation experiments.

2. EXPERIMENT DESIGN AND ANALYSES

2.1 THE HIGH FLUX ISOTOPE REACTOR

The irradiations proposed in this report will be performed with the MiniFuel irradiation vehicle. The MiniFuel irradiation vehicle is designed to be inserted in the inner small vertical experiment facilities (ISVXF) positions within HFIR. HFIR is a pressurized light water–cooled and moderated flux-trap type reactor [14]. The core features highly enriched ^{235}U fuel in aluminum clad, involute fuel plates arranged into two concentric annuli. The core is surrounded by removable and permanent beryllium reflectors, which also feature multiple positions for irradiation experiments, including the ISVXF positions. Experiments are cooled by the moderator, which is between 50 and 60°C. A depiction of the HFIR core layout is shown in Figure 1.

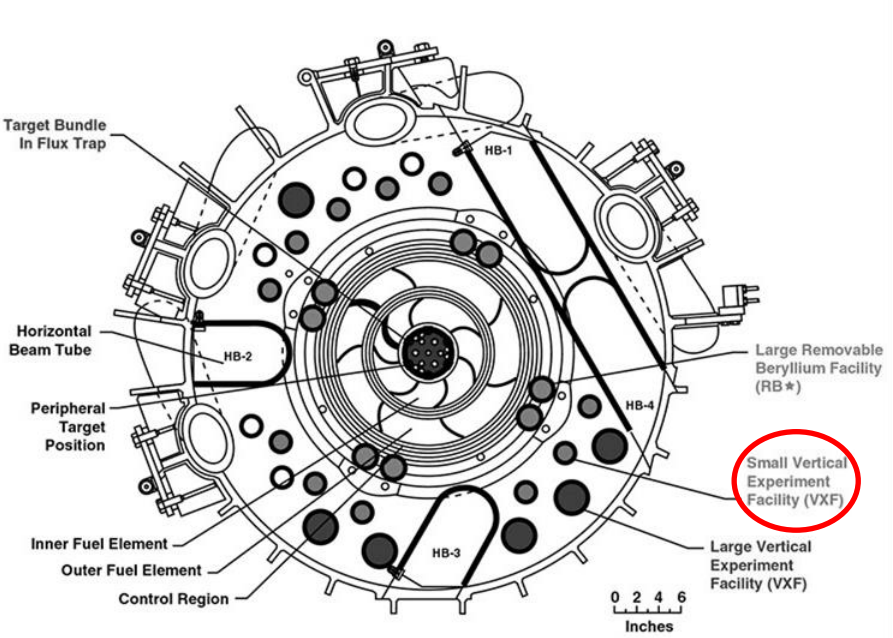

Figure 1. Core layout of HFIR at ORNL [8].

2.2 EXPERIMENT DESIGN

The experiment facility consists of an aluminum basket inserted in the ISVXF which contains individually sealed targets. The experiment basket has three radial positions—two positions facing the toward the core and one position facing away from the core. Each radial position can hold up to three sealed targets, each of which holds up to six subcapsules (54 total). The subcapsules are individually sealed and contain the fuel specimens. Three dimensional (3D) models of the miniature fuel experiment facility are shown in Figure 2. More details on the MiniFuel facility can be found in a prior publication [7].

Placement in the reactor is defined using a radial (R:1–3), axial (A:1–3), subcapsule (S:1–6) (RAS) number, where *R* represents one of the three bore holes within the MiniFuel basket, *A* denotes the target position from bottom to top, and *S* denotes the subcapsule position within the target from bottom to top. The layout of a single radial position with a stack of three targets is shown in Figure 2. This experiment design closely resembles those of previous miniature fuel experiments that were used to irradiate bare fuel kernels, fuel disks, and fully ceramic encapsulated coated particles. A new subcapsule assembly design was built to accommodate miniature TRISO compacts. The subcapsule assembly is also shown in Figure 2. The 3D models were built with CREO 3D modeling software and imported into the neutronic and thermal analysis software packages, HFIRCON and ANSYS, respectively.

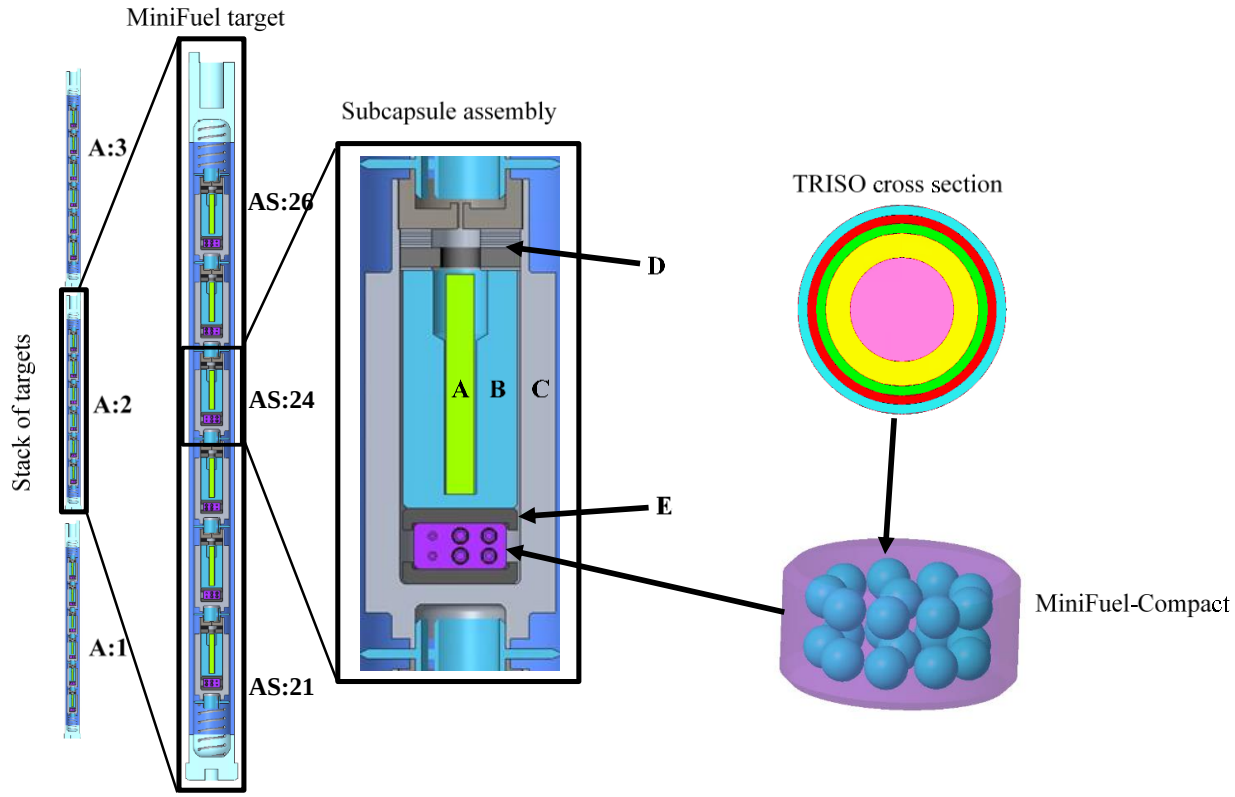

Figure 2. CAD rendering and component summary of the MiniFuel experiment target. The subcapsule's components are labeled (A) SiC thermometry, (B) Mo insert tube, (C) subcapsule, (D) graphite and grafoil disks, and (E) SiC spacer.

2.2.1 Subcapsule Design

The subcapsule is made of molybdenum (Mo) and features a welded Mo endcap to seal the contents in an inert gas (typically helium) and to retain any fission products that may be released in the event of fuel failure. Each subcapsule will contain 20 TRISO particles compacted in a carbon matrix (600 total). With the peak compact approaching 1000°C during irradiation, there is potential for Mo-C interactions and carbide formation. Therefore, two SiC spacers are used to center the compact away from the internal wall of the Mo subcapsule and to provide a barrier between the subcapsule bottom and the Mo insert. The Mo insert's primary purpose is to provide a relatively substantial amount of photonic heating, minimizing the ratio of total fission heating to photon heating in each subcapsule. Minimizing this ratio will reduce temporal changes in specimen temperatures that arise from burnup-induced changes in fission density during irradiation. Graphite foil (grafoil) disks are added to insulate the components and to apply slight compression to the internal components. This not only will reduce unwanted shifting of components during handling but also will increase the contact pressure between the insert tube, spacers, compact, and subcapsule floor, consequently decreasing the interfacial thermal resistance. A SiC thermometer is located inside the Mo insert to measure the capsule temperature using post-irradiation dilatometry [15, 16]. Finally, a graphite disk is added to capture fission products in the event of fuel failure. These components and assemblies are all described in detailed mechanical drawings, available upon request.

2.2.2 Compact Geometry

Each compact was modeled to contain 20 TRISO particles, and the height and diameter of the compacts were modeled as 2.30 and 4.60 mm, respectively. The dimensions of fuel kernels from the AGR lots have

been measured in previous reports [9]. Table 1 summarizes the particle dimensions. Unlike in previous miniature fuel designs –which often relied on cups and fuel dishes to hold the fuel specimens in a fixed arrangement– it would not be feasible in this design to precisely control the placement of individual fuel particles during compaction. Automatically generating a randomized arrangement was considered, but it was expected that the particles would arrange in a pattern like that of the lowest energy state, hexagonal close packing (HCP). Therefore, an HCP-like solid model was manually built and is considered a reasonable approximation of the physical arrangement. The variations in particle arrangement and size were briefly studied early in the design phase and were determined to have some effect on the specimen temperatures. However, this effect is expected to be relatively small compared with the effect of fission heat changes caused by fuel burnup. Sensitivity studies to determine this effect on performance are outside the scope of this report, though placement of the particles can be measured by x-ray computed tomography and is included in as-built sensitivity analyses prior to irradiation [17].

Table 1. AGR TRISO dimensions and the dimensions used in this report [9, 18, 19, 20, 21, 22, 23].

	AGR-2 mean and standard deviation		**Modeled**
	UCO	**UO_2**	**UCO, NUCO & UO_2***
Kernel diameter [µm]	426.7 ± 8.8	507.7 ± 11.9	425
Buffer thickness [µm]	98.9 ± 8.4	97.7 ± 9.9	100
IPyC thickness [µm]	40.4 ± 2.5	41.9 ± 3.2	40
SiC thickness [µm]	35.2 ± 1.2	37.5 ± 1.2	35
OPyC thickness [µm]	43.4 ± 2.9	45.6 ± 2.4	40

*****The larger size of the UO_2 kernels was accounted for by scaling the heat generation rate.

IPyC = inner pyrolytic carbon, OPyC = outer pyrolytic carbon

2.3 NEUTRONIC ANALYSIS

Neutronic calculations were completed to determine heat generation rates in the fuel and target structure from neutron and gamma interactions. These heat generation rates were then provided as inputs for the thermal finite element models and were used to predict the burnup during the irradiation. The analyses were completed using an ORNL-maintained code package, HFIRCON, which serves as an automated, parallelized coupling tool for Monte Carlo N-Particle (MCNP) transport simulations and SCALE's ORIGEN code for activation and decay calculations [24, 25]. The MCNP models were based on the existing HFIR model with cycle 400 experiment loading [26]. Modifications were made to the existing model to include the irradiation experiments described in this report.

The neutronic analyses calculate heat generation from fission neutrons (prompt and delayed), prompt fission photons, delayed photons from fission product decay, alpha and beta decay heat, and photon heating from local activation product decay. The methodology is further described in previous work, so it is only briefly summarized herein [7, 27]. Prompt fission neutron and photon heating was calculated using an established fission neutron source distribution (with neutron and photon tracking) to determine a fission photon source distribution, which is used to calculate the heat generation in all experiment components. Fission product decay photons originating in the HFIR fuel are calculated with a separate calculation. This calculation uses a fixed photon source distribution that reflects the gamma emission rate and spectrum from the accumulated fission products [27]. Activation and decay calculations were performed with ORIGEN using problem-specific cross section data generated from MCNP reaction rates and flux tallies in the fuel specimens. These effective cross sections were provided to the COUPLE cross

section processing module to evaluate burnup and transmutation over the desired number of irradiation cycles using ORIGEN. They yielded local alpha and beta decay heating (assumed to be locally deposited) from activation products, as well as activation product gamma emission rates and spectra. The latter information was used to construct a local activation gamma source distribution for a final MCNP calculation assessing heat generation in the experimental capsule components from activation gammas.

This technique was implemented to assess heat generation and burnup accumulation for the first cycle of irradiation and was extended to assess later irradiation cycles. This was accomplished with automated coupling of flux magnitude and spectral results from MCNP to ORIGEN for depletion and decay assessment, followed by updating of the MCNP models using the isotopics determined from ORIGEN [27].

2.3.1 Target Geometry

Most of the experiment components were manually replicated in MCNP from the ORNL engineering drawings. The experiment assembly consisted of the Al-6061 basket located at the ISVXF-15 position. The three radially arranged bores (R positions) within the basket each contained three full targets with a full loading of similar subcapsules containing fuel. Although the as-built targets will feature TRISO particles of varying size and arrangement, the effect of different fuel loadings on the neutronic performance was expected to be minimal. Therefore, three separate simulations were completed for the three types of fuels considered. This approach also contributed useful data related to the compacts' neutronic performance at other locations that were not planned for the experiment described in this report.

The assembly is oriented such that two radial positions are equidistant from the core, allowing for the highest incident flux on radial positions R:2 and R:3 (with R:1 being ~15% lower). Figure 3 shows a top-down cross section of the facility representation in MCNP, and Figure 4 shows a vertical cross section. The compact specimen—detailing all 20 fuel particles including the SiC, pyrolytic carbon (PyC), and buffer layers—would be difficult to generate by hand in MCNP. The geometry was therefore converted from the CREO geometric format to the MCNP geometry using the ANSYS DesignModeler module. Figure 5 shows the model of the compact in the computer-assisted drawing (CAD) and MNCP rendering. The particle layout was manually generated but can be modified to account for more random distributions using x-ray computed tomography.

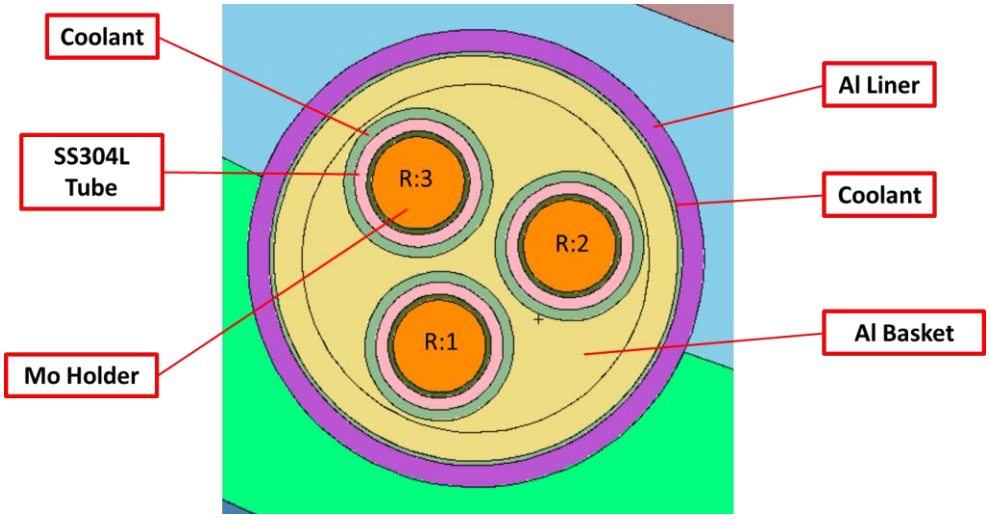

Figure 3. Top-down cross section of experimental assembly in MCNP.

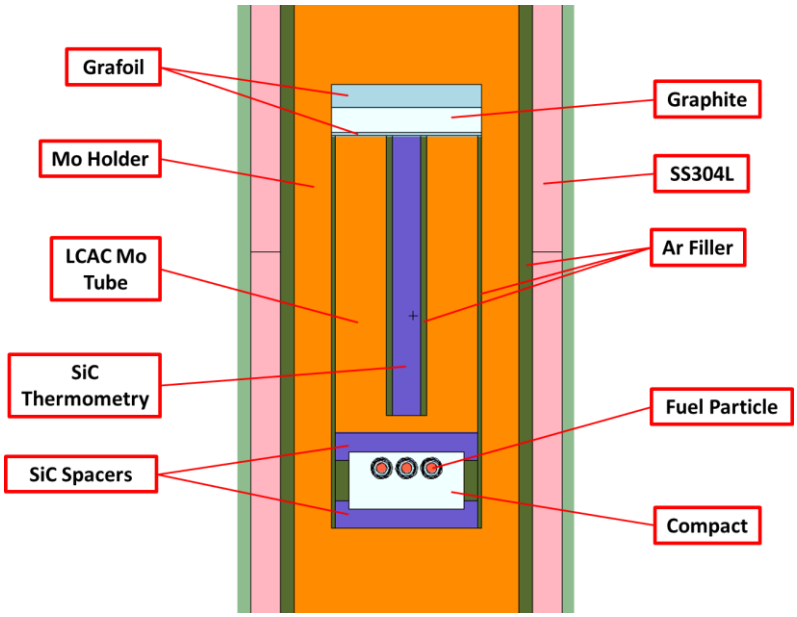

Figure 4. Vertical cross section of experimental assembly in MCNP.

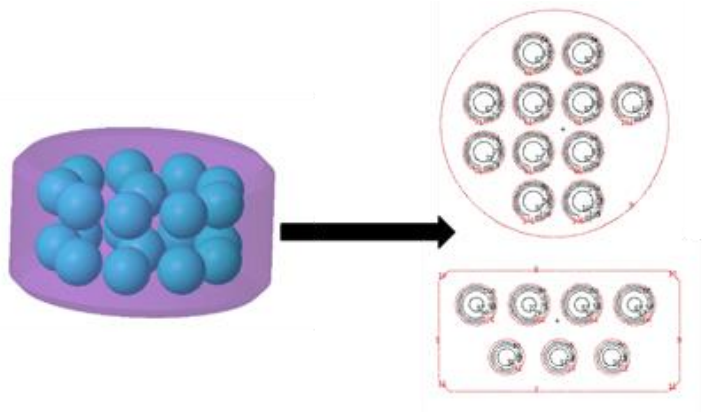

Figure 5. Depiction of conversion from CAD to MCNP using ANSYS.

2.4 THERMAL ANALYSES

Thermal analyses were completed using the finite element software package in ANSYS with a set of custom, internally maintained macros. The macros are used to define material properties and determine thermal contact conductance between components, as well as heat transfer through variable gas gaps. These gas gaps change, depending on the bodies' temperatures and the defined thermal expansion; the solution methodology is referenced in the work by McDuffee [28].

The 3D CAD model was directly imported into ANSYS, where features like fillets and welds were simplified and minor components were removed to reduce the complexity of meshing. Figure 6 shows the CAD target model used for thermal analyses.

Figure 6. The model of the full-length target and subcapsules used for thermal analysis.

2.4.1 Boundary Conditions

Material-dependent heat generation rates were applied to the components using the values determined in the neutronic analyses. Convective boundary conditions on the target housing have been calculated in RELAP5 for previous MiniFuel irradiations in the ISVXF. The heat transfer coefficient used was 44.8 kW/m^{2}K, and the water temperature was calculated to be 58°C [7, 29]. The neutron, gamma, and decay heat generation rates were processed and imported directly from the HFIRCON outputs. The gamma heating rates, q_γ, were approximated with a Gaussian-like equation that is dependent on the axial location, z, and time into the cycle, t, at each ISVXF position:

$$q_\gamma(component, t, z) = q_0(t)\, e^{-\frac{z^2}{\sigma(t)^2}}. \quad (1)$$

During operation, the flux profile of HFIR changes because of fuel burnup and movements of the control rods. Thus, the peak heat generation rates, q_0, and the peaking factors, σ, also vary with time into the cycle. Each subcapsule component type (e.g., thermometry, subcapsule, endcap) in the desired radial basket position was fitted with Eq. (1) at each time step of the HFIRCON simulation data to approximate the peak heat generation rate for each component with respect to time. Then, the average value of the peaking factor across all non-fuel components with respect to time was calculated and used for this analysis, as the gamma heating profile has minimal variation with respect to material. For intermediate timesteps, linear interpolation was automatically applied using the existing time step data. This scheme allowed for the application of an axially varying heat generation rate in ANSYS, which accounted for heat generation gradients across individual components. Since the axial position of TRISO kernels within a single compact varied by less than 1 mm, position dependence was assumed to be negligible. Instead, the kernel-averaged fission heat generation rate in each compact calculated with HFIRCON was discretely applied to each compact, depending on the desired position.

2.4.2 Material Properties

Table 2 summarizes the target structural components and their corresponding materials. The Irradiation Engineering group at ORNL maintains an internally reviewed and updated property database with corresponding ANSYS macro files for setting properties during analyses. These properties include temperature and, in some cases, dose- or fluence-dependent physical properties. The properties are typically taken from MatWeb [30], CINDAS [31], and other literature references. These property files are available upon request. The material properties for the carbon materials in the TRISO particles were taken from the PARFUME Theory and Model Basis Report [32], which includes the PyC layers, buffer layer, and compact. The assumed densities of these components are summarized in Table 3, using AGR-2 as a reference [9]. Some properties, like the matrix thermal conductivity, are dependent on the fluence. These values were calculated using the average flux is each position over four cycles. The average flux results are shown in Table 5, and the fluence with respect to time is detailed in Appendix C.

Table 2. Summary of materials and components

Material	Components	Property references
Molybdenum	Subcapsules, insert tubes	[30, 31]
Ti6Al4V	Centering thimbles	[30, 31]
Silicon carbide	Thermometry, and spacers, SiC TRISO layer	[31, 33]
304 Stainless steel	Target housing	[31]
Grafoil	Insulating disk	[34]
Graphite	Fission product sink	[31, 30, 35]
PyC/carbon matrix	PyC, buffer, matrix	[32]
UO_2	UCO, NUCO, and UO_2 kernels	[36, 37]

Table 3. Assumed densities for TRISO components [9]

	AGR-2 specified range (actual mean) [g/cm^3]		Modeled
	UCO	**UO_2**	**NUCO, UCO & UO_2**
Kernel	>10.4 (10.966 ± 0.033)	>10.4 (10.858 ± 0.082)	10.4
Buffer	1.05 ± 0.10 (not measured)	1.05 ± 0.10 (0.99)	1.05
IpyC	1.90 ± 0.05 (1.89 ± 0.011)	1.90 ± 0.05 (1.89 ± 0.011)	1.9
SiC	>3.19 (3.197 ± 0.004)	>3.19 (3.199)	3.21
OPyC	1.90 ± 0.05 (1.907±0.007)	1.90 ± 0.05 (1.884 ± 0.004)	1.9
Matrix	>1.45 (1.589±0.005)	>1.45 (1.680 ± 0.00)	1.63

Table 4. Average flux for fluence dependent matrix properties

S	Average flux (>0.18 MeV) [n/cm^2/s]			
1	**A:3**	1.87E+14	**A:2**	2.40E+14
2		1.70E+14		2.47E+14
3		1.48E+14		2.50E+14
4		1.25E+14		2.49E+14
5		1.01E+14		2.45E+14
6		7.55E+13		2.36E+14

2.5 EXPERIMENT TEST MATRIX

The experiment test matrix features three different design temperatures, which are defined as the TAVA SiC layer temperature. The two targets nearest to the HFIR center, RA:22 and RA:32, consist of subcapsules that contain alternating NUCO and UCO kernels. These targets were designed to have design temperatures of 500 and 700°C. RA:12 is located behind the other two targets relative to the HFIR radial center, and it contains alternating UO_2 and UCO kernels at 900°C. Two targets also located at RA:23 and RA:33 contain UCO kernels at 500 and 700°C, respectively. The test matrix, subcapsule diameters, and target fill gases are summarized in Table 5.

Table 5. The experiment test matrix summary.

500°C design temperature				700°C design temperature			
	S	**OD (mm)**	**Kernel**		**S**	**OD (mm)**	**Kernel**
RA:23	6	8.90	UCO	**RA:33**	6	8.44	UCO
	5	9.12	UCO		5	8.80	UCO
	4	9.24	UCO		4	8.98	UCO
Ne equivalent	3	9.34	UCO	**22–78% He-Ar**	3	9.12	UCO
	2	9.42	UCO		2	9.22	UCO
	1	9.46	UCO		1	9.28	UCO
RA:22	6	9.36	NUCO	**RA:32**	6	8.58	NUCO
	5	9.60	UCO		5	9.16	UCO
	4	9.37	NUCO		4	8.64	NUCO
Ne equivalent	3	9.60	UCO	**Ne equivalent**	3	9.18	UCO
	2	9.36	NUCO		2	8.58	NUCO
	1	9.57	UCO		1	9.08	UCO

900°C design temperature			
	S	**OD (mm)**	**Kernel**
RA:12	6	9.28	UO_2
	5	9.30	UCO
	4	9.34	UO_2
Ar	3	9.30	UCO
	2	9.30	UO_2
	1	9.25	UCO

3. RESULTS AND DISCUSSION

3.1 NEUTRONIC ANALYSIS RESULTS

The HFIRCON results were processed to provide key variables such as fission rate, photon heating, neutron heating, and fuel burnup for each component. Figure 7 shows the time-dependent burnup during irradiation in HFIR for the three fuel types in their anticipated loading positions within the MiniFuel vehicle. The differences in flux at positions R:2 and R:3 are insignificant, so results for R:3 are represented by the same line as R:2 for illustration purposes in Figure 7. Each line in the plot represents a subcapsule position within an RA position. RA:22 and 32 have a mix of both UCO and NUCO, so three

lines are shown for each for composition, representing each S position. The UCO-fueled particles at A:2 positions exhibit a tighter range of burnups compared with the A:3 positions as a result of the flatter flux profile near the HFIR axial midplane. RA:23 and 33 positions are represented by the black dash-dot line with the lowest line representing the S:6 position. The subcapsule position furthest from the axial midplane, AS:26, has a ~20% reduction in burnup relative to the AS:31 position. The flux profile also results in lower heat generation rates near the reactor's axial periphery, as shown in Figure 8.

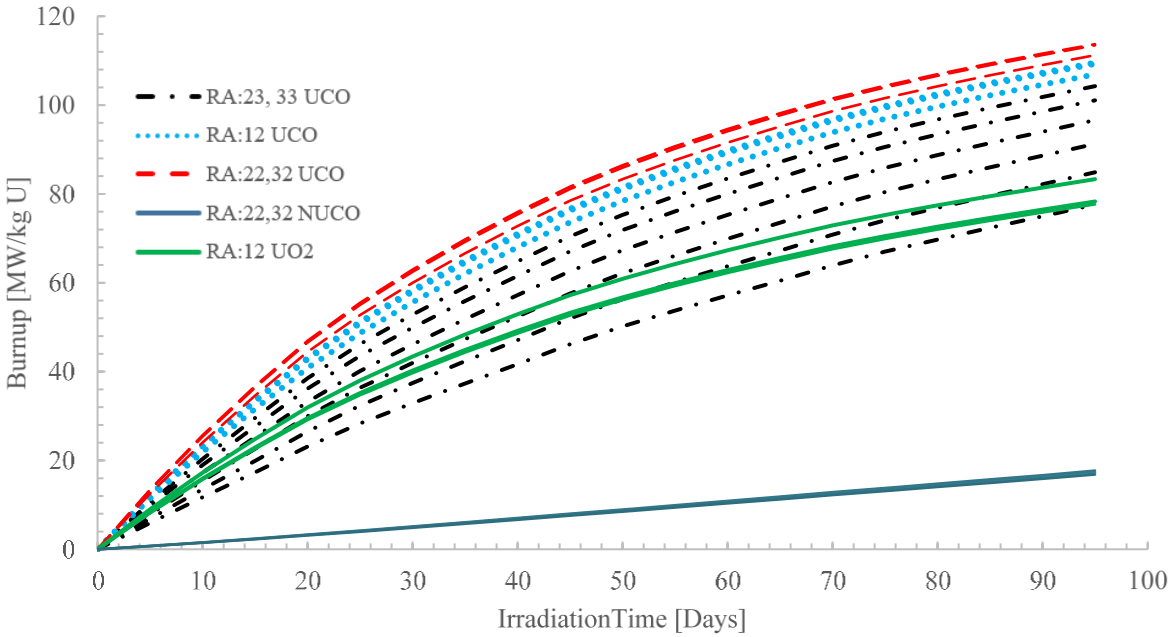

Figure 7. Burnup of the experiment fuel types in planned MiniFuel loading positions.

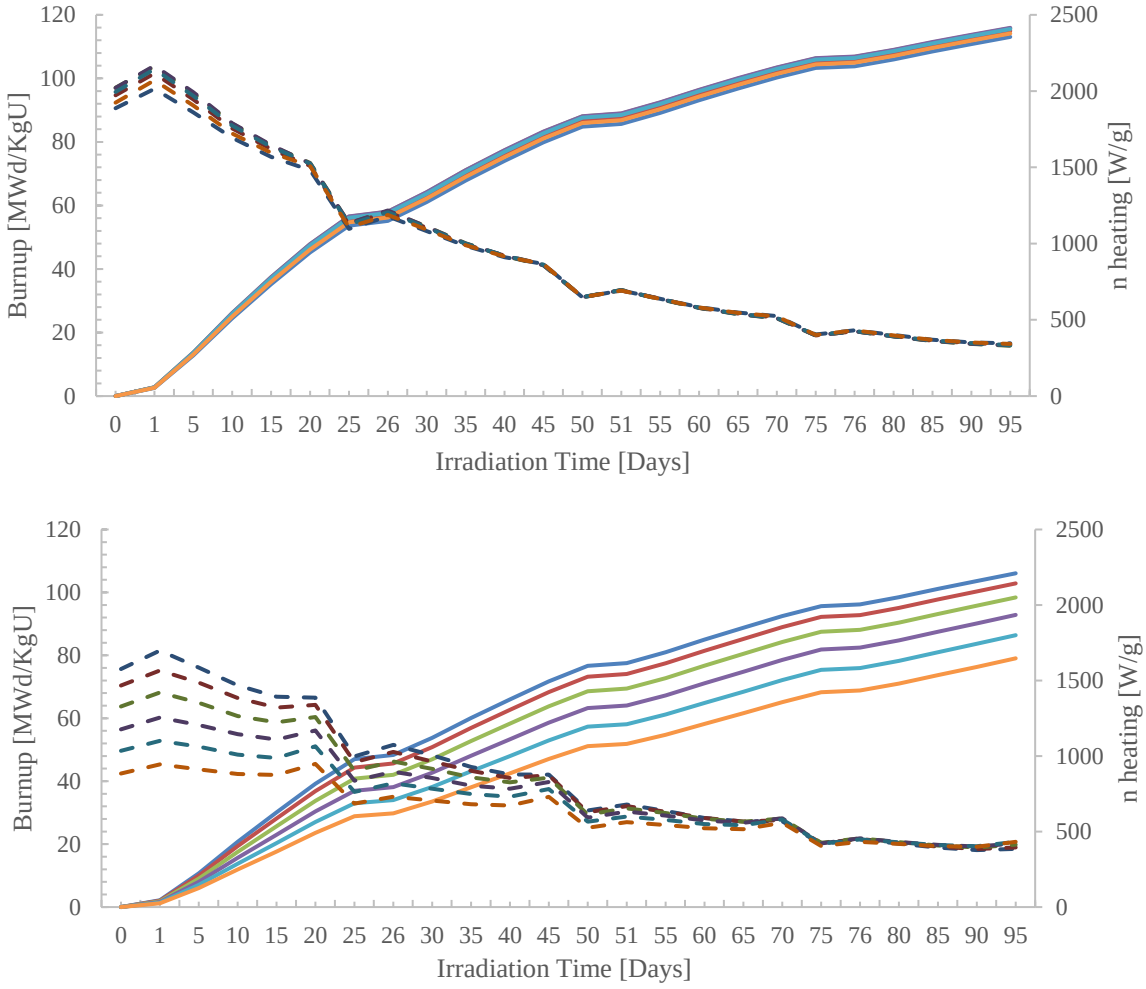

Figure 8. UCO burnup (solid lines) and neutron heat generation rates (dotted lines) at RA:22 (top) vs. RA:23 (bottom), where each line represents an individual S position.

3.2 THERMAL ANALYSIS RESULTS

The thermal analysis was completed for four cycles using 10-day time steps. Figure 9 shows the instantaneous volume-averaged SiC temperature in each compact (top) and the end of irradiation TAVA SiC temperatures versus the fuel burnup (bottom). TAVA temperature swings ranging from ~120 to 180°C were found on the SiC layers in the UCO-bearing compacts, with the larger swings corresponding to the higher design temperature targets and those closer to the axial midplane. These swings were due to the large variations in neutron heat generation rates as the fuel burned up, with maximum burnup achieved at the location of highest flux during irradiation (the reactor axial midplane). Despite these relatively large temporal temperature changes, after the first cycle, the SiC temperature in UCO-bearing compacts generally fluctuates at ±25 °C owing to cyclic effects of the reactor during each irradiation cycle. The reason is the rapid burnup of UCO and reduction in the ^{235}U fission rate relative to the total capsule heat generation rate. Table 6 shows the summarized results for the SiC temperatures in each target for this irradiation campaign.

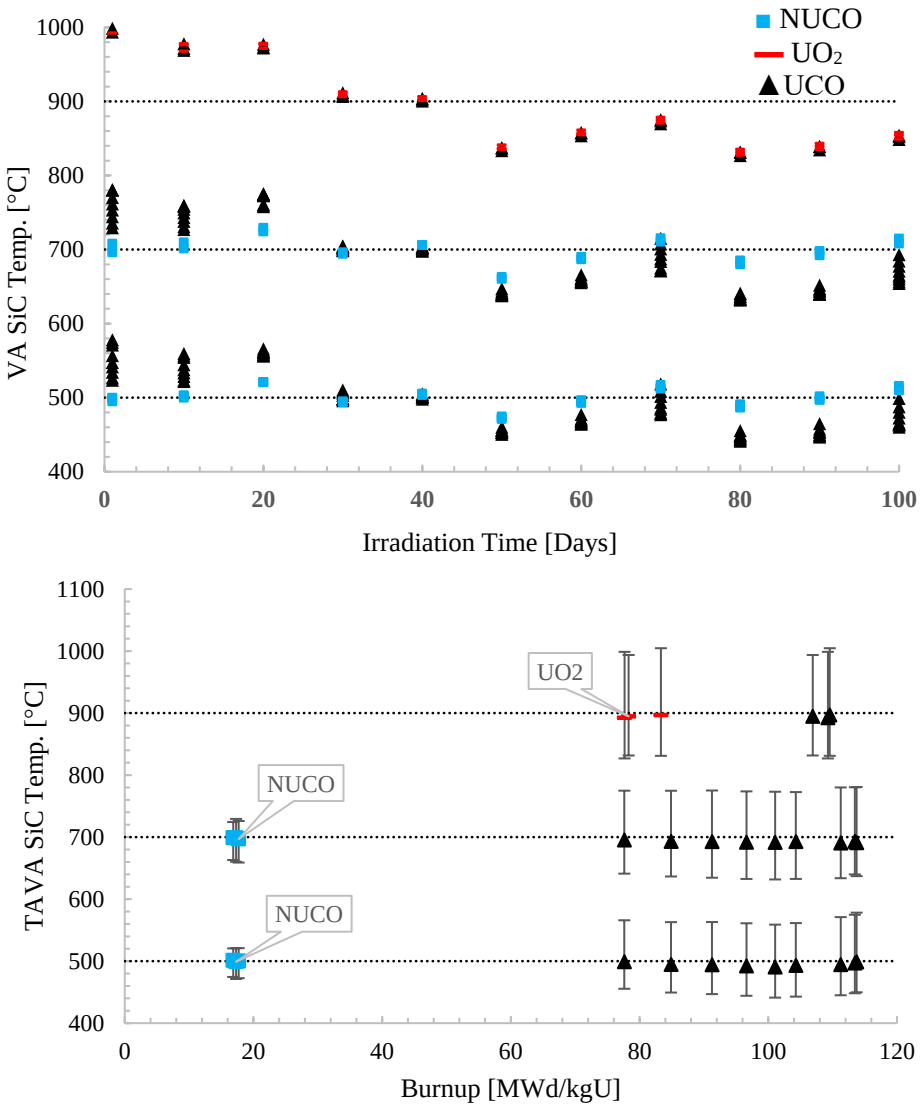

Figure 9. The volume-averaged SiC temperature in each compact with respect to time (top) and the end of irradiation time-averaged, volume-averaged SiC temperatures vs. the fuel burnup (bottom).

Table 6. Thermal result summary of TRISO SiC layer.

Temperatures (°C)		1	2	3	4	5	6
RA: 22	Time average SiC temp	485	497	489	497	486	493
	SiC Max temp	561	516	569	516	565	511
	SiC Min temp	437	471	440	472	438	469
	Temp difference	124	46	129	45	127	42
RA:23	Time average SiC temp	485	483	485	487	486	489
	SiC max temp	551	550	552	554	552	553
	SiC min temp	436	435	438	441	442	447
	Temp difference	115	115	114	113	110	106
RA: 32	Time average SiC temp	673	690	675	688	676	682
	SiC max temp	764	718	766	715	765	707
	SiC min temp	616	652	620	651	622	647
	Temp difference	148	66	146	64	143	59
RA:33	Time average SiC temp	677	679	678	679	677	675
	SiC max temp	757	760	760	761	759	755
	SiC min temp	618	619	620	621	620	620
	Temp difference	139	141	140	140	139	135
RA:12	Time average SiC temp	885	892	888	888	884	884
	SiC max temp	985	997	996	1001	990	985
	SiC min temp	820	827	822	819	818	820
	Temp difference	164	170	174	183	172	165

UO_2

NUCO

UCO

The thermal analysis results used nominal part dimensions and simplified the distribution and sizes of particles within a compact. Following component inspection and fabrication, the model created for this analysis will be refined to improve the predicted specimen temperature. The fuel compacts will undergo dimensional inspection as well as x-ray computed tomography characterization to capture kernel sizes and distributions within the compact. These data will be used to analyze the effect particle size and distribution has on the local temperatures.

4. CONCLUSIONS

High-power-density TRISO fuel is being planned for irradiation in HFIR. The irradiation experiments discussed in this report will support fuel qualification of TRISO for the KP-FHR, under development by Kairos Power, which will have higher operating particle powers but lower temperatures than HTGR designs. A set of experiments was designed using the MiniFuel vehicle to irradiate 30 TRISO-containing carbon matrix compacts at ISVXF in HFIR. Each compact will contain 20 TRISO particles, consisting of 14% enriched UCO, NUCO, or 9.6% enriched UO_2 fuel kernels with time-averaged SiC layer temperature goals of 500, 700 and 900°C. This report summarizes the vehicle designs, neutronic analyses, and thermal analyses completed in support of these irradiation experiments. These analyses show that MiniFuel compact irradiation is a versatile experiment that can be used to study a range of TRISO particle powers and fuel types while still providing reasonable separation of burnup and temperature effects. The TRISO compact irradiation can be leveraged for more irradiations to support other advanced reactor designs using coated particle fuels.

5. AKNOWLEDGMENTS

This work was completed under the DOE Nuclear Science User Facility program in collaboration with Kairos Power, LLC.

6. REFERENCES

[1] D. Petti, "The DOE advanced gas reactor fuel development and qualification program," *JOM*, vol. 61, pp. 62-66, 2010.

[2] N. R. Brown, "A review of in-pile fuel safety tests of TRISO fuel forms and future," *Journal of Nuclear Materials*, vol. 534, no. 152139, 2020.

[3] K. A. Terrani, L. L. Snead and J. C. Gehin, "Microencapsulated fuel technology for commercial light water and advanced reactor application," *Journal of Nuclear Materials*, vol. 427, no. 1-3, pp. 209-224, 2012.

[4] L. L. Snead, "Key differences in the fabrication, irradiation and high temperature accident testing of US and German TRISO-coated particle fuel, and their implications on fuel performance," *Journal of Nuclear Materials*, vol. 448, no. 1-3, pp. 389-398, 2014.

[5] R. Latta, "High Power Irradiation Testing of TRISO Particles in Miniature Fuel Specimens in HFIR," *Transactions*, vol. 121, no. 1, pp. 641-643, 2019.

[6] J. T. Maki, "The challenges associated with high burnup, high temperature and acclerated iradiation for TRISO-coated particle fuel," *Journal of Nuclear Materials*, vol. 371, pp. 270-280, 2007.

[7] C. M. Petrie, "Separate effects irradiation testing of miniature fuel specimens," *Journal of Nuclear Materials*, vol. 526, 2019.

[8] "High Flux Isotope Reactor Technical Parameters," Oak Ridge National Laboratory, [Online]. Available: https://neutrons.ornl.gov/hfir/parameters.

[9] B. Collin, "INL/EXT-14-32277 Rev. 4: AGR-2 Irradiation Test Final As-Run Report," Idaho National Laboratory, Idaho Falls, 2018.

[10] B. Collin, "INL-EXT-10-18097: AGR-1 Irradiation Test Final As-Run Report," Idaho National Laboratory, 2015.

[11] B. Pham, J. Sterbentz, G. Hawkes, D. Scates and J. Palmer, "INL/EXT-19-55429 Rev. 1: AGR-5/6/7 Experiment Monitoring and Simulation Progress," Idaho National Laboratory, 2020.

[12] F. Rice, "Ceramography of Irradiated TRISO fuel from the AGR-2 experiment," *Nuclear Engineerign and Design*, vol. 329, pp. 73-81, 2018.

[13] J. Hunn, "Initial examination of fuel compacts and TRISO particles from the AGR-2 irradiation tests," *Nuclear Engineering and Design*, vol. 329, pp. 89-101, 2017.

[14] R. Cheverton and T. Sims, "ORNL-4621, HFIR Core Nuclear Design," Oak Ridge National Laboratory, Oak Ridge, TN, 1971.

[15] K. Field, J. McDuffee, J. Geringer, C. Petrie and Y. Kato, "Evaluation of the continuous dilatometer method of silicon carbide thermometry for passive irradiation temperature determination," *Nuclear Instruments and Methods in Physics Research Section B: Beam Interactions with Materials and Atoms*, vol. 445, pp. 46-56, 2019.

[16] A. Campbell, A. Porter, Y. Kato and L. Snead, "Method for analyzing passive silicon carbide thermometry with a continuous dilatometer to determine irradiation temperature," *Nuclear Instruments and Methods in Physics Research Section B: Beam Interactions with Materials and Atoms*, vol. 370, pp. 49-58, 2016.

[17] G. W. Helmreich, "Method for measurement of TRISO kernel and layer volumes by X-ray conputed tomography," *Journal of Nuclear Materials,* vol. 539, 2020.

[18] BWXT, "Industrial Fuel Fabrication and Development Lot G73H-10-93085B," 2009.

[19] BWXT, "Industrial Fuel Fabrication and Development Lot G73J-14-93071A, G73J-14-93073A, G73J-14-93074A," 2008.

[20] J. Hunn, F. Montgomery and P. Pappano, "ORNL/TM-2010/017, Rev. 1: Data Compilation for AGR-2 UCO Variant Compact Lot LEU09-OP2-Z," Oak Ridge National Laboratory, 2010.

[21] J. Hunn, F. Montgomery and P. Pappano, "ORNL/TM-2010/055, Rev. 1 :Data Compilation for AGR-2 B&W UO2 Compact Lot LEU11-OP2-Z," Oak Ridge National Laboratory, 2010.

[22] J. Hunn, "ORNL/TM-2009/255: Data Compilation for AGR-2 B&W UO2 Coated Particle Batch G73H-10-93085B," Oak Ridge National Laboratory, 2010.

[23] J. Hunn, "ORNL/TM-2008/134:Data Compilation for AGR-2 Baseline Coated Particle Batch G73J-14-93073A," Oak Ridge National Laboratory, 2008.

[24] X.-5. M. C. Team, "LA-UR-03-1987: MCNP-A General Purpose Monte Carlo N-Particle Transport Code, Version 5," Los Alamos National Laboratory, 2003.

[25] "ORNL/TM-2005/39: SCALE, A Modular Code System for Performing Standardized Computer Analyses for Licensing Evaluation," Oak Ridge National Laboratory, Oak Ridge, TN, 2009.

[26] N. Xoubi and T. Primm, "ORNL/TM-2004/251: Modeling of the High Flux Isotope Reactor Cycle 400," Oak Ridge National Laboratory, Oak Ridege, TN, 2005.

[27] D. Chandler, "Development of an Efficient Approach to Perform Neutronics Simulations for Plutonium-238 Production," in *PHYSOR2016,* Sun Valley, ID, 2016.

[28] J. McDuffee, "Heat transfer through small moveable gas gaps in a multi-body system using the ANSYS finite element software," in *ASME 2013 Heat Transfer Summer Conference collocated with the ASME 2013 7th International Conference on Energy Sustainability and the ASME 2013 11th International Conference on Fuel Cell Science, Engineering and Technology.*, 2013.

[29] L. Ott, G. Bell, R. Ellis, J. McDuffee and R. Morris, "Irradiation of SiC clad fuel in the HFIR," in *Proceedings of Top Fuel 2013,* Charlotte, NC, 2013.

[30] M. LLC, "Material property data," MatWeb, [Online]. Available: http://www.matweb.com. [Accessed 2020].

[31] "CINDAS, LLC: global benchmark for critically evaluated materials properties," CINDAS, LLC, [Online]. Available: http://cindasdata.com..

[32] G. Miller, D. Petti, J. Maki, D. Knudson and Skerjanc, "INL/EXT-18-14497 Rev.1: PARFUME theory and model basis report," Idaho National Laboratory, 2018.

[33] L. L. Snead, "Handbook of SiC properties for fuel performance modeling," *Journal of Nuclear Materials,* vol. 371, no. 1-3, pp. 329-377, 2007.

[34] Graftech, "Grafoil Engineering Manual, second ed.," 2002. [Online]. Available: http://www.graftech.com/wp-content/uploads/2014/12/GRAFOIL-Engineering-Manual-2nd-Ed.pdf.

[35] T. Burchell, D. Felde and K. Thoms, "Experimental Plan and Preliminary Design Report for HFIR High Temperature Graphite Irradiation Capsules HTV-1 and 2, ORNL-GEN4/LTR-05-013," Oak Ridge National Laboratory, Oak Ridge, TN, 2005.

[36] L. Siefken, E. Coryell, A. Harvego and J. Hohorst, "SCDAP/RELAP5/MOD 3.3 Code Manual: MATPRO - A Library of Material Properties for Light-Water-Reactor Accident Analysis, NUREG/CR-6150, vol. 4," U.S. Nuclear Regulatory Commission, Washington, DC, 2001.

[37] D. Lanning, C. Beyer and K. Geelhood, "FRAPCON-3 Updates, Including Mixed-Oxide Fuel Properties, NUREG/CR-6534," Nuclear Regulatory Commission, Washington, DC.

APPENDIX A. FISSION RATE DENSITY

APPENDIX A. FISSION RATE DENSITY

This section contains the fission rate density output from HFIRCON in fissions/cm^3/s

	RAS	231	232	233	234	235	236
	Fuel	UCO	UCO	UCO	UCO	UCO	UCO
	0	6.32948E+14	5.86766E+14	5.30455E+14	4.69685E+14	4.10268E+14	3.53964E+14
	1	6.76733E+14	6.27731E+14	5.65636E+14	5.02932E+14	4.39496E+14	3.76381E+14
	5	6.36044E+14	5.92327E+14	5.39333E+14	4.81555E+14	4.21972E+14	3.67394E+14
	10	5.87819E+14	5.5425E+14	5.04269E+14	4.5626E+14	4.04173E+14	3.53254E+14
	15	5.56753E+14	5.27202E+14	4.88676E+14	4.4317E+14	3.94999E+14	3.47557E+14
	20	5.55514E+14	5.36366E+14	5.05143E+14	4.68953E+14	4.25812E+14	3.78776E+14
	25	3.97552E+14	3.80501E+14	3.5751E+14	3.31186E+14	3.04442E+14	2.71974E+14
	26	4.28121E+14	4.09583E+14	3.85218E+14	3.57592E+14	3.24806E+14	2.92818E+14
	30	4.01685E+14	3.8562E+14	3.6448E+14	3.4088E+14	3.12917E+14	2.84051E+14
	35	3.70564E+14	3.60624E+14	3.43942E+14	3.22922E+14	2.97298E+14	2.72592E+14
	40	3.5249E+14	3.42644E+14	3.30225E+14	3.13587E+14	2.90549E+14	2.67498E+14
Time (days)	**45**	3.51947E+14	3.48425E+14	3.41565E+14	3.32118E+14	3.13973E+14	2.91163E+14
	50	2.5295E+14	2.49591E+14	2.43284E+14	2.35054E+14	2.25208E+14	2.10308E+14
	51	2.7355E+14	2.70561E+14	2.6375E+14	2.54251E+14	2.40982E+14	2.24529E+14
	55	2.56747E+14	2.53663E+14	2.49691E+14	2.41628E+14	2.31643E+14	2.15531E+14
	60	2.37379E+14	2.37002E+14	2.33616E+14	2.30714E+14	2.21026E+14	2.08742E+14
	65	2.26731E+14	2.27361E+14	2.25719E+14	2.23649E+14	2.17102E+14	2.06843E+14
	70	2.28135E+14	2.33699E+14	2.36208E+14	2.3554E+14	2.33549E+14	2.23988E+14
	75	1.6585E+14	1.67361E+14	1.6832E+14	1.69201E+14	1.68243E+14	1.62635E+14
	76	1.81223E+14	1.81694E+14	1.82435E+14	1.82855E+14	1.79541E+14	1.72781E+14
	80	1.6915E+14	1.71105E+14	1.72783E+14	1.73237E+14	1.71708E+14	1.6708E+14
	85	1.58177E+14	1.59853E+14	1.63564E+14	1.64164E+14	1.64679E+14	1.60659E+14
	90	1.52423E+14	1.54213E+14	1.58246E+14	1.60998E+14	1.61947E+14	1.60082E+14
	95	1.53756E+14	1.58314E+14	1.6511E+14	1.70558E+14	1.7426E+14	1.74267E+14

RAS	221	222	223	224	225	226
Fuel	UCO	NUCO	UCO	NUCO	UCO	NUCO
0	7.57377E+14	4.23414E+13	8.13927E+14	4.34323E+13	8.0381E+14	4.12562E+13
1	8.07724E+14	4.55499E+13	8.67219E+14	4.66539E+13	8.59868E+14	4.43424E+13
5	7.42787E+14	4.56678E+13	7.95253E+14	4.67959E+13	7.87179E+14	4.42614E+13
10	6.80619E+14	4.88432E+13	7.16702E+14	5.02166E+13	7.1074E+14	4.69635E+13
15	6.31334E+14	5.30899E+13	6.57348E+14	5.44165E+13	6.54733E+14	5.10212E+13
20	5.94492E+14	5.78161E+13	6.11542E+14	5.8759E+13	6.1079E+14	5.5699E+13
25	4.33707E+14	4.88076E+13	4.46805E+14	4.99234E+13	4.45431E+14	4.70908E+13
26	4.70661E+14	5.9185E+13	4.84821E+14	6.03943E+13	4.82643E+14	5.70139E+13
30	4.33134E+14	5.60325E+13	4.45977E+14	5.69902E+13	4.44558E+14	5.41089E+13
35	3.9416E+14	5.59152E+13	4.00732E+14	5.69213E+13	4.00034E+14	5.41988E+13
40	3.64685E+14	5.78263E+13	3.6669E+14	5.8759E+13	3.6886E+14	5.6519E+13
45	3.45717E+14	6.07394E+13	3.44786E+14	6.20402E+13	3.45064E+14	5.94062E+13
50	2.55636E+14	5.04619E+13	2.54623E+14	5.22332E+13	2.54016E+14	4.96861E+13
51	2.7849E+14	6.06057E+13	2.78529E+14	6.26606E+13	2.78028E+14	5.96104E+13
55	2.5682E+14	5.72966E+13	2.54646E+14	5.88659E+13	2.542E+14	5.63012E+13
60	2.34913E+14	5.70665E+13	2.32029E+14	5.83689E+13	2.3208E+14	5.59296E+13
65	2.18917E+14	5.83866E+13	2.14905E+14	5.97086E+13	2.16396E+14	5.71708E+13
70	2.10444E+14	6.12557E+13	2.03191E+14	6.23055E+13	2.0509E+14	5.98779E+13
75	1.57764E+14	5.09507E+13	1.53501E+14	5.20818E+13	1.53396E+14	4.97605E+13
76	1.73951E+14	6.10123E+13	1.69528E+14	6.23124E+13	1.70091E+14	5.94283E+13
80	1.59993E+14	5.77327E+13	1.55286E+14	5.90998E+13	1.55588E+14	5.59499E+13
85	1.4818E+14	5.69944E+13	1.43484E+14	5.84366E+13	1.43715E+14	5.57209E+13
90	1.4107E+14	5.87731E+13	1.36035E+14	6.02583E+13	1.36513E+14	5.75074E+13
95	1.37688E+14	6.17624E+13	1.3117E+14	6.34862E+13	1.32699E+14	6.08078E+13

RAS	331	332	333	334	335	336
Fuel	UCO	UCO	UCO	UCO	UCO	UCO
0	6.39768E+14	5.92977E+14	5.36679E+14	4.75564E+14	4.16905E+14	3.60111E+14
1	6.83217E+14	6.3076E+14	5.74111E+14	5.06996E+14	4.44339E+14	3.81023E+14
5	6.40977E+14	5.9923E+14	5.41395E+14	4.85391E+14	4.28127E+14	3.71302E+14
10	5.91033E+14	5.54295E+14	5.1071E+14	4.60636E+14	4.07965E+14	3.57608E+14
15	5.58303E+14	5.31482E+14	4.90211E+14	4.45824E+14	4.01116E+14	3.52649E+14
20	5.56193E+14	5.37164E+14	5.07955E+14	4.71824E+14	4.30572E+14	3.83658E+14
25	3.97365E+14	3.81231E+14	3.61216E+14	3.34445E+14	3.06235E+14	2.75004E+14
26	4.31868E+14	4.11369E+14	3.88461E+14	3.60673E+14	3.27654E+14	2.91166E+14
30	4.02829E+14	3.87288E+14	3.67233E+14	3.42147E+14	3.15204E+14	2.84092E+14
35	3.72352E+14	3.62374E+14	3.44243E+14	3.2354E+14	3.01359E+14	2.72134E+14
40	3.52681E+14	3.44087E+14	3.32244E+14	3.14628E+14	2.93258E+14	2.6836E+14
45	3.5255E+14	3.50017E+14	3.4161E+14	3.30932E+14	3.14866E+14	2.93428E+14
50	2.52786E+14	2.49885E+14	2.45128E+14	2.36941E+14	2.25669E+14	2.11459E+14
51	2.73966E+14	2.6989E+14	2.64131E+14	2.536E+14	2.41261E+14	2.25125E+14
55	2.55619E+14	2.53766E+14	2.49659E+14	2.43104E+14	2.32038E+14	2.18794E+14
60	2.35782E+14	2.37067E+14	2.34918E+14	2.29197E+14	2.21936E+14	2.10048E+14
65	2.26476E+14	2.2693E+14	2.26197E+14	2.22795E+14	2.15439E+14	2.07263E+14
70	2.27609E+14	2.29962E+14	2.34246E+14	2.37088E+14	2.32825E+14	2.24746E+14
75	1.64095E+14	1.65137E+14	1.67979E+14	1.6911E+14	1.67519E+14	1.63743E+14
76	1.79485E+14	1.8061E+14	1.82095E+14	1.82658E+14	1.80233E+14	1.73538E+14
80	1.67284E+14	1.69389E+14	1.71104E+14	1.72786E+14	1.72239E+14	1.68148E+14
85	1.56852E+14	1.58181E+14	1.62011E+14	1.64559E+14	1.64482E+14	1.62206E+14
90	1.50937E+14	1.53488E+14	1.5759E+14	1.60377E+14	1.61378E+14	1.60183E+14
95	1.52323E+14	1.57854E+14	1.64374E+14	1.69324E+14	1.72843E+14	1.734E+14

RAS	321	322	323	324	325	326
Fuel	UCO	NUCO	UCO	NUCO	UCO	NUCO
0	7.60931E+14	4.24396E+13	8.15873E+14	4.35718E+13	8.06573E+14	4.14556E+13
1	8.12693E+14	4.52446E+13	8.72832E+14	4.68214E+13	8.61769E+14	4.45545E+13
5	7.48575E+14	4.56009E+13	7.96961E+14	4.69267E+13	7.94527E+14	4.4762E+13
10	6.82567E+14	4.82732E+13	7.20116E+14	4.97477E+13	7.13369E+14	4.77289E+13
15	6.27601E+14	5.23376E+13	6.58776E+14	5.43429E+13	6.54909E+14	5.15272E+13
20	5.95905E+14	5.67623E+13	6.11937E+14	5.90113E+13	6.13895E+14	5.621E+13
25	4.35073E+14	4.83222E+13	4.473E+14	5.07022E+13	4.47304E+14	4.71227E+13
26	4.70514E+14	5.81717E+13	4.8718E+14	6.16593E+13	4.84021E+14	5.71351E+13
30	4.33726E+14	5.51688E+13	4.45994E+14	5.81091E+13	4.43817E+14	5.41512E+13
35	3.94983E+14	5.48718E+13	4.01548E+14	5.83519E+13	4.01561E+14	5.44304E+13
40	3.64359E+14	5.65674E+13	3.69354E+14	6.01328E+13	3.69463E+14	5.63487E+13
45	3.46742E+14	5.99759E+13	3.44024E+14	6.22975E+13	3.44497E+14	5.97073E+13
50	2.55501E+14	4.99125E+13	2.55885E+14	5.18921E+13	2.54474E+14	4.93388E+13
51	2.78258E+14	6.00788E+13	2.78518E+14	6.25345E+13	2.78413E+14	5.98175E+13
55	2.56472E+14	5.69952E+13	2.5421E+14	5.90083E+13	2.55608E+14	5.59036E+13
60	2.35226E+14	5.63007E+13	2.33451E+14	5.90417E+13	2.3182E+14	5.58692E+13
65	2.19763E+14	5.78079E+13	2.15955E+14	6.03279E+13	2.15929E+14	5.75652E+13
70	2.11521E+14	6.08279E+13	2.03119E+14	6.26676E+13	2.05102E+14	6.09009E+13
75	1.57007E+14	5.07307E+13	1.53711E+14	5.23118E+13	1.52793E+14	5.05374E+13
76	1.73285E+14	6.0691E+13	1.70108E+14	6.28125E+13	1.69361E+14	6.04654E+13
80	1.6001E+14	5.72145E+13	1.55454E+14	5.95838E+13	1.55628E+14	5.68749E+13
85	1.47782E+14	5.67005E+13	1.43907E+14	5.90322E+13	1.44076E+14	5.6271E+13
90	1.411E+14	5.82462E+13	1.36683E+14	6.07079E+13	1.36988E+14	5.82306E+13
95	1.37093E+14	6.11239E+13	1.31591E+14	6.32353E+13	1.32388E+14	6.16145E+13

RAS	121	122	123	124	125	126
Fuel	UCO	UO2	UCO	UO2	UCO	UO2
0	6.80889E+14	4.6321E+14	7.28475E+14	5.03804E+14	7.21543E+14	4.53967E+14
1	7.23941E+14	4.92359E+14	7.71939E+14	5.35633E+14	7.65849E+14	4.82249E+14
5	6.7095E+14	4.56794E+14	7.15128E+14	4.96133E+14	7.09225E+14	4.48278E+14
10	6.15219E+14	4.16985E+14	6.49498E+14	4.49774E+14	6.44641E+14	4.10592E+14
15	5.77001E+14	3.88439E+14	6.04026E+14	4.19778E+14	6.00162E+14	3.84044E+14
20	5.51471E+14	3.69885E+14	5.68461E+14	3.95843E+14	5.66218E+14	3.67143E+14
25	4.09302E+14	2.77541E+14	4.25753E+14	2.97084E+14	4.21747E+14	2.7461E+14
26	4.42048E+14	3.01209E+14	4.57867E+14	3.22065E+14	4.55073E+14	2.96691E+14
30	4.0979E+14	2.77551E+14	4.21438E+14	2.96219E+14	4.19273E+14	2.74732E+14
35	3.76615E+14	2.54902E+14	3.8465E+14	2.714E+14	3.85312E+14	2.53531E+14
40	3.52881E+14	2.37645E+14	3.57344E+14	2.52787E+14	3.56273E+14	2.37528E+14
45	3.3671E+14	2.28482E+14	3.35673E+14	2.40808E+14	3.36864E+14	2.28674E+14
50	2.51973E+14	1.72859E+14	2.52869E+14	1.82134E+14	2.52832E+14	1.71618E+14
51	2.72821E+14	1.88663E+14	2.74613E+14	1.9927E+14	2.73689E+14	1.87967E+14
55	2.52497E+14	1.75519E+14	2.53026E+14	1.8361E+14	2.52651E+14	1.74459E+14
60	2.32083E+14	1.61424E+14	2.31099E+14	1.69501E+14	2.31895E+14	1.61643E+14
65	2.19133E+14	1.52926E+14	2.16653E+14	1.58681E+14	2.17054E+14	1.53192E+14
70	2.1227E+14	1.47964E+14	2.05097E+14	1.53803E+14	2.07912E+14	1.4878E+14
75	1.60266E+14	1.14181E+14	1.57115E+14	1.17743E+14	1.57748E+14	1.13645E+14
76	1.74631E+14	1.26346E+14	1.71471E+14	1.30639E+14	1.72115E+14	1.26057E+14
80	1.61861E+14	1.17525E+14	1.58919E+14	1.2094E+14	1.6016E+14	1.17193E+14
85	1.50333E+14	1.09754E+14	1.47101E+14	1.13493E+14	1.48178E+14	1.0967E+14
90	1.43019E+14	1.05519E+14	1.39397E+14	1.08835E+14	1.40352E+14	1.05569E+14
95	1.39264E+14	1.04466E+14	1.34636E+14	1.06634E+14	1.35758E+14	1.04697E+14

APPENDIX B. SIC LAYER TEMPERATURES

APPENDIX B. SIC LAYER TEMPERATURES

This section summarizes the volume-averaged SiC layer temperature over all 20 particles in each compact with respect to irradiation time.

		SiC layer average temperature (°C)					
	T(days)	**S1**	**S2**	**S3**	**S4**	**S5**	**S6**
	1	561	493	569	494	565	485
	10	545	498	551	498	547	491
	20	546	516	548	516	545	511
	30	497	491	500	492	497	487
	40	492	501	495	502	491	497
RA: 22	50	445	471	448	472	446	469
	60	457	492	460	493	458	490
	70	468	511	469	511	468	509
	80	437	486	440	487	438	485
	90	441	496	445	497	442	495
	100	450	509	453	510	451	508
	1	547	539	533	527	517	513
	10	536	529	526	521	514	511
	20	551	550	552	554	552	553
	30	494	491	491	491	487	488
	40	492	490	492	494	493	495
RA:23	50	446	444	447	449	449	453
	60	459	457	460	463	463	468
	70	476	479	486	493	499	507
	80	436	435	438	441	442	447
	90	441	440	444	448	450	456
	100	457	458	465	473	479	489
	1	764	695	766	691	765	677
	10	743	698	744	694	743	683
	20	744	718	742	715	743	707
	30	685	686	687	684	687	677
	40	680	697	682	695	683	689
RA: 32	50	621	652	623	651	624	647
	60	638	679	640	678	642	674
	70	653	703	655	700	657	699
	80	616	673	620	672	622	670
	90	622	685	627	684	629	683
	100	636	701	639	699	642	699
	1	754	748	740	731	719	709
	10	739	736	730	724	715	706
RA:33	20	757	760	760	761	759	755
	30	689	689	687	686	682	678
	40	687	688	688	688	686	683

		SiC layer average temperature (°C)					
	T(days)	**S1**	**S2**	**S3**	**S4**	**S5**	**S6**
	50	625	627	628	629	628	627
	60	642	644	645	646	645	645
	70	668	674	680	686	691	694
	80	618	619	620	621	620	620
	90	625	627	628	629	630	630
	100	647	652	657	663	668	672
	1	985	997	996	1001	990	985
	10	961	971	969	972	963	961
	20	965	972	968	970	963	964
	30	899	906	903	903	898	898
	40	894	900	897	895	892	893
RA:12	50	827	833	829	827	824	826
	60	847	853	849	847	845	846
	70	865	871	865	863	861	864
	80	820	827	822	819	818	820
	90	828	835	830	826	825	828
	100	843	850	844	840	840	844

APPENDIX C. FAST FLUX VALUES

APPENDIX C. FAST FLUX VALUES

	RAS Fast Flux (>0.18 MeV) n/cm^2/s					
Days	**221**	**222**	**223**	**224**	**225**	**226**
0	2.338E+14	2.414E+14	2.459E+14	2.443E+14	2.407E+14	2.312E+14
1	2.411E+14	2.501E+14	2.524E+14	2.521E+14	2.467E+14	2.373E+14
5	2.407E+14	2.473E+14	2.511E+14	2.503E+14	2.452E+14	2.361E+14
10	2.394E+14	2.468E+14	2.504E+14	2.490E+14	2.448E+14	2.350E+14
15	2.415E+14	2.481E+14	2.515E+14	2.513E+14	2.455E+14	2.366E+14
20	2.454E+14	2.506E+14	2.532E+14	2.522E+14	2.481E+14	2.394E+14
25	2.329E+14	2.403E+14	2.443E+14	2.439E+14	2.392E+14	2.303E+14
26	2.414E+14	2.483E+14	2.510E+14	2.511E+14	2.461E+14	2.371E+14
30	2.392E+14	2.465E+14	2.500E+14	2.500E+14	2.440E+14	2.355E+14
35	2.395E+14	2.466E+14	2.502E+14	2.484E+14	2.443E+14	2.345E+14
40	2.416E+14	2.486E+14	2.503E+14	2.499E+14	2.451E+14	2.361E+14
45	2.438E+14	2.500E+14	2.520E+14	2.506E+14	2.472E+14	2.401E+14
50	2.333E+14	2.405E+14	2.447E+14	2.438E+14	2.396E+14	2.307E+14
51	2.407E+14	2.485E+14	2.519E+14	2.512E+14	2.457E+14	2.362E+14
55	2.398E+14	2.471E+14	2.503E+14	2.488E+14	2.450E+14	2.358E+14
60	2.389E+14	2.460E+14	2.488E+14	2.478E+14	2.442E+14	2.345E+14
65	2.405E+14	2.472E+14	2.505E+14	2.496E+14	2.451E+14	2.362E+14
70	2.449E+14	2.498E+14	2.526E+14	2.507E+14	2.470E+14	2.388E+14
75	2.329E+14	2.405E+14	2.439E+14	2.441E+14	2.396E+14	2.307E+14
76	2.402E+14	2.479E+14	2.512E+14	2.507E+14	2.462E+14	2.369E+14
80	2.395E+14	2.468E+14	2.504E+14	2.496E+14	2.451E+14	2.356E+14
85	2.390E+14	2.459E+14	2.489E+14	2.488E+14	2.434E+14	2.346E+14
90	2.410E+14	2.476E+14	2.499E+14	2.494E+14	2.450E+14	2.360E+14
95	2.445E+14	2.495E+14	2.518E+14	2.511E+14	2.463E+14	2.390E+14

	RAS Fast Flux (>0.18 MeV) n/cm^2/s					
Days	**231**	**232**	**233**	**234**	**235**	**236**
0	1.853E+14	1.666E+14	1.449E+14	1.224E+14	9.895E+13	7.343E+13
1	1.900E+14	1.694E+14	1.477E+14	1.244E+14	1.008E+14	7.485E+13
5	1.889E+14	1.683E+14	1.465E+14	1.237E+14	9.961E+13	7.409E+13
10	1.884E+14	1.685E+14	1.468E+14	1.240E+14	1.002E+14	7.515E+13
15	1.902E+14	1.704E+14	1.487E+14	1.250E+14	1.010E+14	7.583E+13
20	1.970E+14	1.785E+14	1.566E+14	1.334E+14	1.081E+14	8.113E+13
25	1.854E+14	1.662E+14	1.449E+14	1.217E+14	9.881E+13	7.386E+13
26	1.887E+14	1.691E+14	1.469E+14	1.239E+14	9.989E+13	7.434E+13
30	1.881E+14	1.682E+14	1.460E+14	1.230E+14	9.932E+13	7.397E+13
35	1.887E+14	1.682E+14	1.472E+14	1.238E+14	9.978E+13	7.488E+13
40	1.899E+14	1.702E+14	1.479E+14	1.250E+14	1.007E+14	7.558E+13
45	1.970E+14	1.774E+14	1.565E+14	1.330E+14	1.079E+14	8.053E+13
50	1.858E+14	1.664E+14	1.452E+14	1.228E+14	9.853E+13	7.399E+13

51	1.885E+14	1.691E+14	1.473E+14	1.234E+14	9.981E+13	7.475E+13
55	1.884E+14	1.682E+14	1.465E+14	1.239E+14	9.947E+13	7.413E+13
60	1.876E+14	1.675E+14	1.462E+14	1.234E+14	9.916E+13	7.414E+13
65	1.894E+14	1.694E+14	1.482E+14	1.252E+14	1.010E+14	7.529E+13
70	1.972E+14	1.777E+14	1.567E+14	1.327E+14	1.071E+14	8.030E+13
75	1.854E+14	1.655E+14	1.449E+14	1.221E+14	9.925E+13	7.363E+13
76	1.886E+14	1.688E+14	1.475E+14	1.238E+14	1.002E+14	7.477E+13
80	1.883E+14	1.678E+14	1.460E+14	1.234E+14	9.970E+13	7.431E+13
85	1.872E+14	1.676E+14	1.460E+14	1.229E+14	9.919E+13	7.421E+13
90	1.898E+14	1.689E+14	1.481E+14	1.252E+14	1.008E+14	7.548E+13
95	1.965E+14	1.770E+14	1.562E+14	1.328E+14	1.074E+14	8.013E+13

	RAS Fast Flux (>0.18 MeV) n/cm^2/s					
Days	**121**	**122**	**123**	**124**	**125**	**126**
0	1.988E+14	2.054E+14	2.074E+14	2.071E+14	2.039E+14	1.970E+14
1	2.054E+14	2.115E+14	2.143E+14	2.132E+14	2.096E+14	2.021E+14
5	2.039E+14	2.101E+14	2.129E+14	2.121E+14	2.082E+14	2.003E+14
10	2.036E+14	2.095E+14	2.115E+14	2.110E+14	2.076E+14	1.999E+14
15	2.050E+14	2.108E+14	2.134E+14	2.124E+14	2.085E+14	2.013E+14
20	2.083E+14	2.127E+14	2.151E+14	2.138E+14	2.101E+14	2.043E+14
25	1.977E+14	2.044E+14	2.073E+14	2.067E+14	2.031E+14	1.968E+14
26	2.046E+14	2.107E+14	2.137E+14	2.127E+14	2.084E+14	2.015E+14
30	2.031E+14	2.089E+14	2.116E+14	2.112E+14	2.069E+14	2.002E+14
35	2.030E+14	2.092E+14	2.115E+14	2.106E+14	2.069E+14	2.002E+14
40	2.048E+14	2.101E+14	2.130E+14	2.123E+14	2.072E+14	2.009E+14
45	2.077E+14	2.125E+14	2.141E+14	2.136E+14	2.097E+14	2.036E+14
50	1.984E+14	2.044E+14	2.074E+14	2.066E+14	2.025E+14	1.966E+14
51	2.041E+14	2.104E+14	2.131E+14	2.121E+14	2.083E+14	2.014E+14
55	2.030E+14	2.094E+14	2.120E+14	2.105E+14	2.072E+14	2.004E+14
60	2.029E+14	2.078E+14	2.111E+14	2.111E+14	2.069E+14	1.999E+14
65	2.043E+14	2.094E+14	2.124E+14	2.115E+14	2.076E+14	2.010E+14
70	2.084E+14	2.128E+14	2.142E+14	2.125E+14	2.099E+14	2.037E+14
75	1.975E+14	2.036E+14	2.068E+14	2.064E+14	2.025E+14	1.962E+14
76	2.043E+14	2.107E+14	2.128E+14	2.127E+14	2.085E+14	2.010E+14
80	2.032E+14	2.087E+14	2.119E+14	2.112E+14	2.071E+14	2.003E+14
85	2.026E+14	2.080E+14	2.106E+14	2.107E+14	2.065E+14	1.993E+14
90	2.038E+14	2.095E+14	2.116E+14	2.109E+14	2.073E+14	2.011E+14
95	2.076E+14	2.122E+14	2.139E+14	2.132E+14	2.094E+14	2.041E+14

	RAS Fast Flux (>0.18 MeV) n/cm^2/s					
Days	**321**	**322**	**323**	**324**	**325**	**326**
0	2.345E+14	2.423E+14	2.456E+14	2.452E+14	2.405E+14	2.325E+14
1	2.423E+14	2.506E+14	2.539E+14	2.524E+14	2.475E+14	2.383E+14
5	2.408E+14	2.478E+14	2.516E+14	2.506E+14	2.457E+14	2.367E+14

10	2.411E+14	2.474E+14	2.506E+14	2.499E+14	2.450E+14	2.357E+14
15	2.414E+14	2.485E+14	2.523E+14	2.511E+14	2.456E+14	2.369E+14
20	2.456E+14	2.510E+14	2.530E+14	2.535E+14	2.488E+14	2.404E+14
25	2.341E+14	2.410E+14	2.445E+14	2.448E+14	2.401E+14	2.321E+14
26	2.413E+14	2.492E+14	2.529E+14	2.515E+14	2.467E+14	2.382E+14
30	2.405E+14	2.476E+14	2.507E+14	2.502E+14	2.449E+14	2.364E+14
35	2.397E+14	2.475E+14	2.515E+14	2.503E+14	2.446E+14	2.363E+14
40	2.421E+14	2.487E+14	2.511E+14	2.509E+14	2.452E+14	2.368E+14
45	2.455E+14	2.508E+14	2.528E+14	2.518E+14	2.482E+14	2.402E+14
50	2.340E+14	2.413E+14	2.453E+14	2.450E+14	2.405E+14	2.315E+14
51	2.420E+14	2.483E+14	2.528E+14	2.515E+14	2.470E+14	2.376E+14
55	2.398E+14	2.474E+14	2.504E+14	2.503E+14	2.447E+14	2.361E+14
60	2.396E+14	2.470E+14	2.503E+14	2.485E+14	2.444E+14	2.354E+14
65	2.413E+14	2.480E+14	2.516E+14	2.495E+14	2.466E+14	2.373E+14
70	2.454E+14	2.512E+14	2.532E+14	2.520E+14	2.474E+14	2.389E+14
75	2.342E+14	2.416E+14	2.449E+14	2.450E+14	2.404E+14	2.310E+14
76	2.412E+14	2.491E+14	2.522E+14	2.515E+14	2.467E+14	2.375E+14
80	2.400E+14	2.477E+14	2.511E+14	2.512E+14	2.458E+14	2.362E+14
85	2.393E+14	2.463E+14	2.494E+14	2.492E+14	2.438E+14	2.359E+14
90	2.417E+14	2.483E+14	2.519E+14	2.496E+14	2.449E+14	2.364E+14
95	2.452E+14	2.514E+14	2.535E+14	2.511E+14	2.474E+14	2.399E+14

	RAS Fast Flux (>0.18 MeV) n/cm^2/s					
Days	**331**	**332**	**333**	**334**	**335**	**336**
0	1.866E+14	1.668E+14	1.454E+14	1.227E+14	9.941E+13	7.429E+13
1	1.903E+14	1.705E+14	1.486E+14	1.247E+14	1.003E+14	7.556E+13
5	1.890E+14	1.694E+14	1.474E+14	1.239E+14	9.997E+13	7.489E+13
10	1.890E+14	1.691E+14	1.477E+14	1.246E+14	1.002E+14	7.488E+13
15	1.907E+14	1.710E+14	1.491E+14	1.261E+14	1.011E+14	7.595E+13
20	1.974E+14	1.790E+14	1.573E+14	1.340E+14	1.084E+14	8.061E+13
25	1.865E+14	1.667E+14	1.448E+14	1.229E+14	9.843E+13	7.395E+13
26	1.902E+14	1.697E+14	1.478E+14	1.246E+14	1.005E+14	7.477E+13
30	1.886E+14	1.691E+14	1.471E+14	1.238E+14	9.963E+13	7.485E+13
35	1.888E+14	1.692E+14	1.475E+14	1.243E+14	1.005E+14	7.481E+13
40	1.903E+14	1.702E+14	1.489E+14	1.255E+14	1.010E+14	7.590E+13
45	1.981E+14	1.790E+14	1.571E+14	1.330E+14	1.080E+14	8.145E+13
50	1.864E+14	1.665E+14	1.451E+14	1.231E+14	9.945E+13	7.424E+13
51	1.901E+14	1.697E+14	1.476E+14	1.245E+14	1.004E+14	7.510E+13
55	1.894E+14	1.688E+14	1.469E+14	1.237E+14	1.001E+14	7.445E+13
60	1.882E+14	1.687E+14	1.466E+14	1.238E+14	1.002E+14	7.492E+13
65	1.903E+14	1.703E+14	1.491E+14	1.255E+14	1.015E+14	7.562E+13
70	1.979E+14	1.788E+14	1.568E+14	1.329E+14	1.079E+14	8.112E+13
75	1.863E+14	1.663E+14	1.458E+14	1.224E+14	9.905E+13	7.417E+13
76	1.898E+14	1.696E+14	1.475E+14	1.244E+14	9.979E+13	7.505E+13

80	1.895E+14	1.692E+14	1.473E+14	1.247E+14	1.007E+14	7.468E+13
85	1.875E+14	1.690E+14	1.472E+14	1.238E+14	9.997E+13	7.455E+13
90	1.906E+14	1.704E+14	1.487E+14	1.253E+14	1.017E+14	7.606E+13
95	1.973E+14	1.787E+14	1.570E+14	1.335E+14	1.079E+14	8.096E+13